

www.acsami.org Research Article

# Highly Tunable Circularly Polarized Emission of an Aggregation-Induced Emission Dye Using Helical Nano- and Microfilaments as Supramolecular Chiral Templates

Jiao Liu, Yann Molard, Marianne E. Prévôt,\* and Torsten Hegmann\*



Cite This: ACS Appl. Mater. Interfaces 2022, 14, 29398-29411



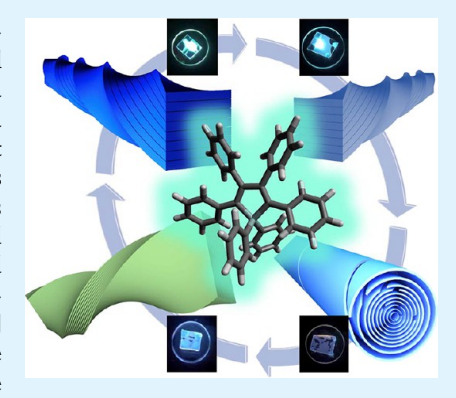
**ACCESS** I

Metrics & More

Article Recommendations

Supporting Information

**ABSTRACT:** Aggregation-induced emission (AIE)-based circularly polarized luminescence (CPL) has been recognized as a promising pathway for developing chiroptical materials with high luminescence dissymmetry factors ( $|g_{lum}|$ ). Here, we propose a method for the construction of a thermally tunable CPL-active system based on a supramolecular self-assembly approach that utilizes helical nano- or microfilament templates in conjunction with an AIE dye. The CPL properties of the ensuing ensembles are predominantly determined by the intrinsic geometric differences among the various filament templates such as their overall dimensions (width, height, and helical pitch) and the area fraction of the exposed aromatic segments or sublayers. The proposed mechanism is based on the collective data acquired by absorption, steady state and time-resolved fluorescence, absolute quantum yield, and CPL measurements. The highest  $|g_{lum}|$  value for the most promising dual-modulated helical nanofilament templates in the present series was further enhanced, reaching up to  $|g_{lum}| = 0.25$  by confinement in the appropriate diameter of anodized aluminum oxide (AAO) nanochannels. It is envisioned



that this methodology will afford new insights into the design of temperature-rate indicators or anti-counterfeiting tags using a combination of structural color by the nano- and microfilament templates and the AIE property of the guest dye.

KEYWORDS: bent-core liquid crystals, helical nanofilaments, B4 phase, circular polarized luminescence, aggregation-induced emission, chiral templating

#### INTRODUCTION

Chirality in molecular architectures and assemblies derives from the dissymmetry of either the building blocks or the environment. Chirality, defined as the inability to superimpose an object onto its mirror image by any kind of translation or rotation,<sup>2</sup> is of significant relevance in chemistry, physics, materials science, and biology among several other fields.<sup>3-7</sup> The control and application of the fascinating chiroptical properties exhibited by chiral systems continues to be an active area of research. 8-11 Circular dichroism (CD) has been extensively used for the investigation of the difference in absorption between the left- and right-handed circularly polarized light. 12,13 Hence, CD provides basic information on the ground-state chiroptical properties of molecules, and its magnitude can be calculated by the dissymmetry factor  $g_{abs}$  =  $2(\varepsilon_{\rm L} - \varepsilon_{\rm R})/(\varepsilon_{\rm L} + \varepsilon_{\rm R})$ , where  $\varepsilon_{\rm L}$  and  $\varepsilon_{\rm R}$  are the molar extinction coefficients of the left- and right-handed circularly polarized light, respectively, based on the underlying absorptive processes. Closely related to CD, circularly polarized luminescence (CPL) gives the excited-state information on the emission difference of left- and right-handed circularly polarized light. The primary criterion for appraising CPL is to calculate the emission (here luminescence) dissymmetry factor  $g_{\text{lum}} = 2(I_{\text{L}} - I_{\text{R}})/(I_{\text{L}} + I_{\text{R}})$ , where  $I_{\text{L}}$  and  $I_{\text{R}}$  are the intensity of the left- and right-handed circularly polarized luminescence, respectively.  $^{14-19}$  The values of CD and CPL, by definition, range from 2 to -2. The maximum value of  $g_{lum} = \pm 2$  means that an ideal left- or right-handed polarization of the emitted light, while a  $g_{lum} = 0$  corresponds to no circular polarization of the luminescence. The photophysical property of CPL echoes structural information of chiral molecules or molecules in chiral environments in their excited states. The key for realizing practical applications of CD and CPL is to attain a high g value. Through irradiation with unpolarized light, CPL can be achieved by chiral molecules or molecules (chiral or achiral) in a chiral environment, and it is valuable for its utility in various photofunctional materials, including 3D displays for chiral sensing as well as for optical information encryption and storage.  $^{20-26}$  Most organic CPL systems tested in solution show  $|g_{lum}|$  values in the range of  $10^{-5}$  to  $10^{-3}$  in magnitude,  $^{27}$ 

Received: March 21, 2022 Accepted: May 25, 2022 Published: June 17, 2022





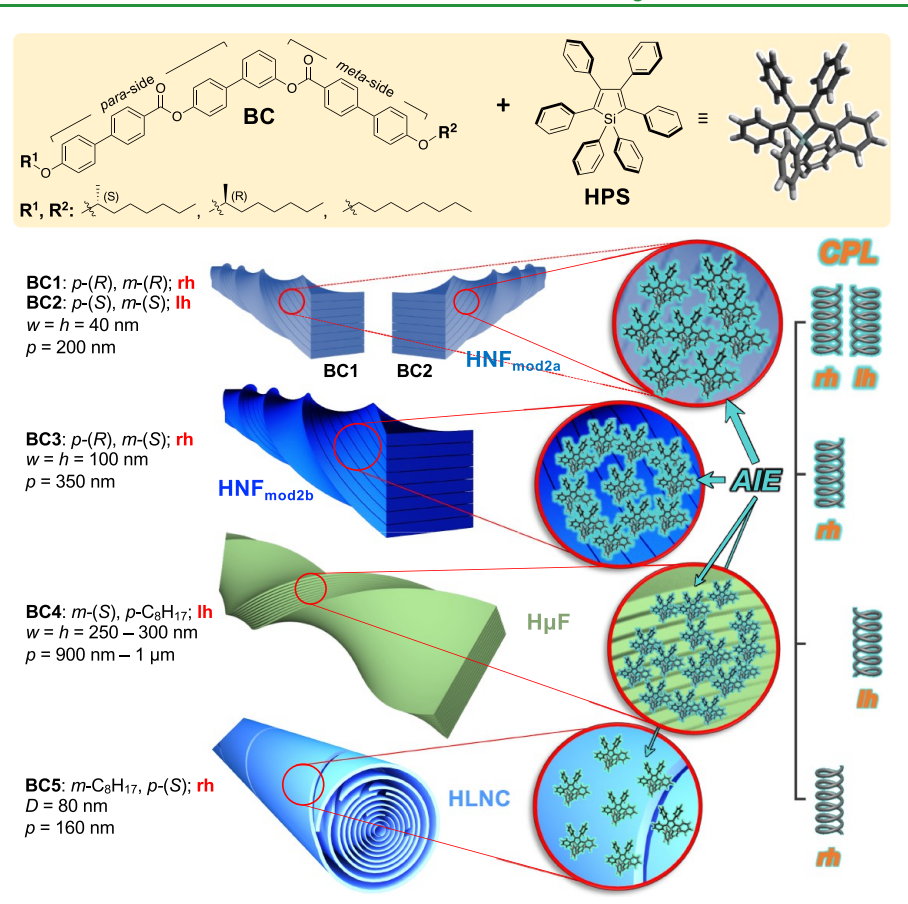


Figure 1. Tris-biphenyl-based BCLC materials BC1–BC5<sup>48–51</sup> forming a range of B4 morphologies depending on the number, position, and relative configuration of the chiral center(s) at C-1 in the aliphatic side chain(s); width (w), height (h), diameter (D), and pitch (p) of the helical/heliconical filament templates are provided; the handedness of the shape is indicated (rh = right-handed; lh = left-handed). Enlarged sections (red circles) show the expected predominant aggregation of HPS in the aromatic domains of the HNF and H $\mu$ F as well as a lack thereof in the HLNC morphology; the anticipated magnitude of the AIE (schematically shown as a luminescent shadow enveloping the HPS molecules with the anticipated magnitude indicated by the arrow width) and the resulting handedness (helices) of the CPL depending on the specific B4 morphology's dimensions and helical pitch are given at the right.

and their performance is often diminished in the solid state due to the notorious aggregation-caused quenching (ACQ) effect. Thus, the design and preparation of chiral AIE systems<sup>28-30</sup> (light emission induced by aggregate formation) is a suitable approach to address this problem. Among AIE systems, hexaphenylsilole (HPS) is emblematic-a well-studied dye, characterized by a fairly strong photoluminescence emission. HPS is a propeller-like luminogen as revealed by crystal structure analysis, with a silole core that is decorated with six phenyl rings forming, in the absence of a chiral bias, a conglomerate of left- and right-handed propellerlike molecules.<sup>30</sup> The molecule takes this conformation due to the torsion between the peripheral phenyl rings and the silole plane. In the solid state, the spatial constrain of silole restricts intramolecular rotational, vibrational, and torsional motions (i.e., RIM), 31,35-41 thereby generating AIE and promoting radiative decays and high luminescent quantum yields (QY). This outcome vanishes in solution where active molecular motions of the AIE systems provide non-radiative relaxation channels, drastically reducing the QY values.

An intriguing recent approach for fabricating CPL-active materials via a self-assembly pathway consisting in associating the guest luminophore to an assembled chiral host and called "chiral host—achiral luminescent guest" has been widely demonstrated. Liu and colleagues reported rigorous research

on CPL materials and proposed a general method for the fabrication of nanoassemblies with CPL properties from achiral dyes or AIE systems. For example, through a supramolecular self-assembly approach using achiral CsPbX<sub>3</sub> perovskite nanocrystals containing different halides (X = Cl, Br, and I) and chiral amine-containing lipid (LGAm/DGAm) gelators, they formed CPL-active perovskite nanocrystals covering a wide range of the visible spectrum by adjustment of the halide. 42 They also proposed a method for the fabrication of full-color-tunable CPL-active quantum dots (QDs) based on the supramolecular self-assembly of achiral QDs by chiral lipid gelators. 43 The mixture of the organic lipid gelator with the core-shell-type QDs modified with achiral 3-mercaptopropionic acid generated the formation of a gel that consisted of nanotube assemblies imparting QD alignment. The versatility of this process arises from tuning the blending ratio of various colorful QDs in a co-gel. 43,44 Ihara's group studied a binary system composed of amphiphilic molecules such as L-glutamic acid derivatives to provide chiral, ordered nanotemplates and a cyanine (NK-2012) fluorescent dye. 45 The tunability of the emission was achieved by the appropriate selection of the dye. Jin et al. reported an inorganic CPL-active "luminescent guest-chiral host" system where luminescent lanthanide oxide (Eu<sub>2</sub>O<sub>3</sub> or Tb<sub>2</sub>O<sub>3</sub>) nanoparticles, acting as guests, were encapsulated into chiral non-helical SiO<sub>2</sub> nanofibers, functioning as host, through calcination of chiral  $SiO_2$  hybrid nanofibers, thereby trapping the lanthanide ions ( $Eu^{3+}$  and  $Tb^{3+}$ ). Recently, the AIE phenomenon has been associated with the geometry of the self-assembly to boost the chiroptical properties of a CPL-active material. It was found that achiral AIE luminophores can be encapsulated into confined nanotubes via organic gelation, which then emit circularly polarized light by direct excitation. The self-active material is a self-active material and the self-active material into confined nanotubes via organic gelation, which then emit circularly polarized light by direct excitation.

In all systems described above, the tunability of the CPL properties is controlled by variation (modification) of the "luminescent guest-chiral host" composition. Using liquid crystals as media in "luminescent guest-chiral host" systems, will allow the dynamic modulation of CPL properties within the structure via an external stimulus such as temperature, solvent, or electric field. It has been shown that common achiral nematic liquid crystal (N-LC, here E7) can be doped by AIE-active (R)/(S)-BINOL-CN enantiomers, and the resulting chiral emissive nematic liquid crystals (N\*-LCs) yield high glum values of aggregation-induced CPL.<sup>28</sup> However, apart from CPL amplification, the tunability of such systems has yet not been explored. Aside from N\*-LCs generating or templating CPL, bent-core LC systems (BCLC) forming now temperature-dependent as well as cooling rate tunable helical nano- or microfilaments<sup>48-52</sup> are yet underutilized.

What has been reported for such helical nanoassemblies is that BCLC-based nanofilaments themselves show fairly low  $g_{\text{lum}}$  values (on the order of  $|g_{\text{lum}}| \approx 10^{-3}$ ). 8,53,54 However, if used as templates, such morphologically chiral nanofilaments can serve as active as well as tunable templates with respect to overall dimensions, helical pitch, surface fraction of exposed aggregation sites, and polymorphism, with all these parameters allowing control over the overall CPL output. To demonstrate such active templating, we here investigate four distinct types of B4 chiral nanotemplates (Figure 1) whose structures and morphologies were previously thoroughly studied and reported. 48-52,55,56 These nanofilament or nanocylinder B4 phase morphologies were realized by strategically incorporating chiral centers in aliphatic side chains at the core-chain junctures in each side chain with identical (BC1 and BC2)<sup>48</sup> or opposite configuration (BC3)<sup>51</sup> or in only one of the side chains, either in the shorter meta-side of the molecule (BC4)<sup>49</sup> or in the longer para-side (BC5). 50 With chiral centers located in each side of the aliphatic chains, a dual-modulated helical nanofilament (HNF<sub>mod2</sub>) phase forms (both upon slow as well as rapid cooling) due to an intralayer mismatch between the top and bottom molecular halves of these bent-core molecules that can only be relieved by local saddle splay with negative Gaussian curvature.<sup>57</sup> The dimensions of these HNFs differ, solely depending on the choice of identical ((p-S)/(m-S)) or (p-R)/(m-R)) versus opposite configuration (p-(R)/m-(S)) of the two chiral centers, i.e., smaller  $HNF_{mod2a}$  for BC1 and BC2 but larger  $HNF_{mod2b}$  for BC3 (Figure 1).<sup>48,51</sup> If the chiral center is located only in the shorter meta-side of the molecule (BC4), the formation of an entirely different phase structure is caused solely by adjusting the cooling rate from the isotropic liquid phase. Upon rapid cooling, a morphology termed helical microfilaments (H $\mu$ F) forms, while slow cooling results in the exclusive formation of an oblique columnar ( $Col_{ob} - p2/m$ ) LC phase. 49 Repositioning the chiral center to the longer paraside of the molecule (BC5) results in the formation of yet another B4 morphology termed heliconical-layered nanocylinders (HLNC) on slow cooling and a coexistence of these HLNCs and a rectangular columnar ( $Col_r - c2mm$ ) phase upon rapid cooling. <sup>50</sup>

To elucidate the ability of these helical BCLC morphologies to serve as active tunable chiral templates for the generation of CPL, we studied binary mixtures of the BCLC molecules giving rise to these morphologies with the HPS. Considering the type of morphology, especially their dimensions, makeup of the exposed interface (aliphatic vs aromatic), and varying helical pitch, one would predict that the underlying subtle changes of the number, position, and configuration of the chiral center(s) in these BCLC molecules should result in significant differences in CPL responses and therefore the magnitude of glum. Furthermore, using an additional level of templating, i.e., using confinement in appropriately sized nanopores of anodic aluminum oxide (AAO) wafers may lead to further enhancement of CPL activity due to the alignment particularly of the smaller and likely most efficient  $\mathsf{HNF}_{\mathsf{mod2a}}$  filament templates for HPS AIE. How these chiral BCLC morphologies in binary mixtures with HPS should in principle compare with respect to AIE-based CPL efficiency is also schematically shown in Figure 1.

# ■ MATERIALS AND METHODS

The synthesis and complete characterization of the five BCLC molecules forming the templates were previously reported by our group.  $^{48-51}$  BC1–BC3 with a chiral center in each of the aliphatic chains form the HNF $_{\rm mod2a}$  (BC1 and BC2), and BC3 forms the larger HNF $_{\rm mod2b}$  morphology either upon slow cooling (at a rate of 5 °C min $^{-1}$ ) or upon thermal quenching to room temperature (rate  $\approx 50$  °C min $^{-1}$ ) each after heating the sample to the isotropic liquid state. The handedness of the HNF $_{\rm mod2a}$  morphology solely depends on the configuration of the two chiral centers; BC3-formed right-handed HNF $_{\rm mod2b}$  based on the configuration is the longer *para*-side of the molecule, as previously reported. BC4 forms the H $\mu$ F morphology exclusively upon rapid cooling (quenching) from the isotropic liquid phase, and BC5 forms the HLNC morphology exclusively upon slow cooling. 1,1,2,3,4,5-Hexaphenyl-1H-silole (HPS) was purchased from Sigma-Aldrich and used as received.

Thin film samples for all spectroscopic measurements were prepared as follows: neat BCLC materials and binary mixtures with HPS were heated to a temperature above the clearing point (i.e., into the isotropic liquid phase at T > 170 °C) and as such sandwiched between precleaned but otherwise untreated quartz substrates (spacing of 10  $\mu$ m) by capillary action. As-prepared samples were subsequently cooled to room temperature ( $T \approx 20$  °C; either on slow cooling at a rate of 5 °C min<sup>-1</sup> or using a rapid thermal quench at a rate of about 50 °C min<sup>-1</sup>; here, especially BC4, which shows polymorphism depending on the cooling rate). Preceding the thermal sample preparation, binary mixtures of BC1-BC5 with an admixed 0.1-0.4 wt % of HPS were prepared by completely dissolving the appropriate amount of each component in chloroform (standardized solutions) and thoroughly mixing these solutions in small glass vials using sonication for 15 min in a standard sonication bath. The solvent was then fully evaporated at T = 60 °C for 5 h.

Polarized optical microscopy (POM) observations were carried out under an Olympus BX3 or a Nikon 80i polarizing microscope each equipped with a Linkam LTS420E hot stage, a Nikon Intensilight irradiation source, a Nikon DS-FI2 digital camera, and an ocean optics QE65000 photodetector connected by optical fiber. The excitation wavelength was selected with a bandwidth of 330–380 nm using an optical filter. POM studies were carried out prior to CPL measurements to further guarantee the absence of significant HPS phase separation. UV–Vis spectra were acquired with an OLIS-Cary 17 spectrophotometer. CPL measurements were accomplished using an OLIS CPL Solo instrument at room temperature using laser excitation at  $\lambda_{\rm exc} = 260$  nm for the neat compounds and  $\lambda_{\rm exc} = 385$  nm for the mixtures containing HPS. The absolute quantum yield (AQY)

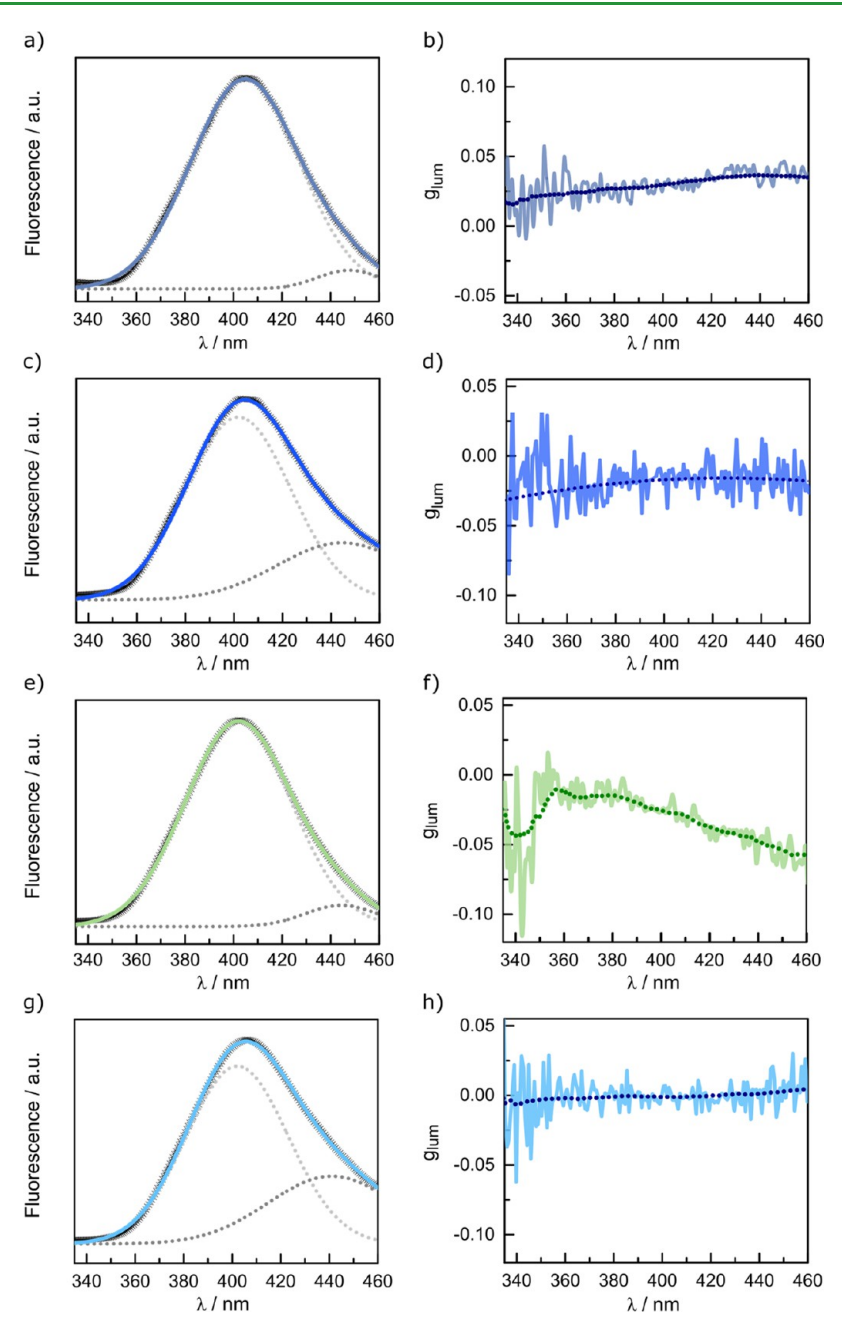


Figure 2. Deconvolution in several Gaussians (in dark and light gray dashed dots) of the emission signal envelope obtained at  $\lambda_{\rm exc}$  = 260 nm (left panel) and  $g_{\rm lum}$  (right panel) vs the wavelengths of (a, b) BC2, (c, d) BC3, (e, f) BC4, and (g, h) BC5. Sample thickness: 10  $\mu$ m films sandwiched between untreated quartz substrates after heating to the isotropic liquid phase (T > 170 °C) and subsequent cooling to room temperature ( $T \approx 20$  °C); plots are color-coded based on the morphology color shown in Figure 1; fluorescence spectra deconvolution shows identical values for  $\lambda_1$  and  $\lambda_2$  for BC2–BC5.

in the solid state was measured using a C9920–03 Hamamatsu system made of an Hg light excitation source, a monochromator, an integrating sphere, and a PMA12 CCD photodetector. The excitation wavelength was set at  $\lambda_{\rm exc}=365$  nm. Lifetime measurements and TRPL mapping at 296 K were acquired using a picosecond laser diode (Jobin Yvon deltadiode) at  $\lambda_{\rm exc}=375$  nm and a Hamamatsu C10910–25 streak camera mounted with a slow single sweep unit. Signals were integrated on the entire emission decay, and fits were calculated using HPDTA software provided by the streak camera manufacturer. The goodness-of-fit was judged by the reduced  $\chi^2$  value and residual plot shape. Scanning electron microscopy (SEM) was performed on a Quanta 450 FEG SEM. Transmission electron microscopy (TEM) was accomplished using a FEI Tecnai TF20 TEM instrument at an accelerating voltage of 200 kV. Small-angle X-ray

scattering (SAXS) experiments were performed with a Xenocs Xeuss 3.0 using a Cu  $K_{\alpha}$  source ( $\lambda = 1.54 \text{ Å}$ ).

# ■ RESULTS AND DISCUSSION

Variations in Template Shape. To characterize the modulation of the CPL properties governed by the five B4 templates differing in morphology, dimensions, helical pitch, and the extent of exposure of aromatic vs aliphatic surface sites, both solid-state fluorescence as well as CPL measurements were performed at one given concentration of HPS. Spectroscopic analysis of the neat BCLC compounds (B4 phases or morphologies) shows that all undoped helical filaments exhibit photoluminescence (PL) properties, includ-

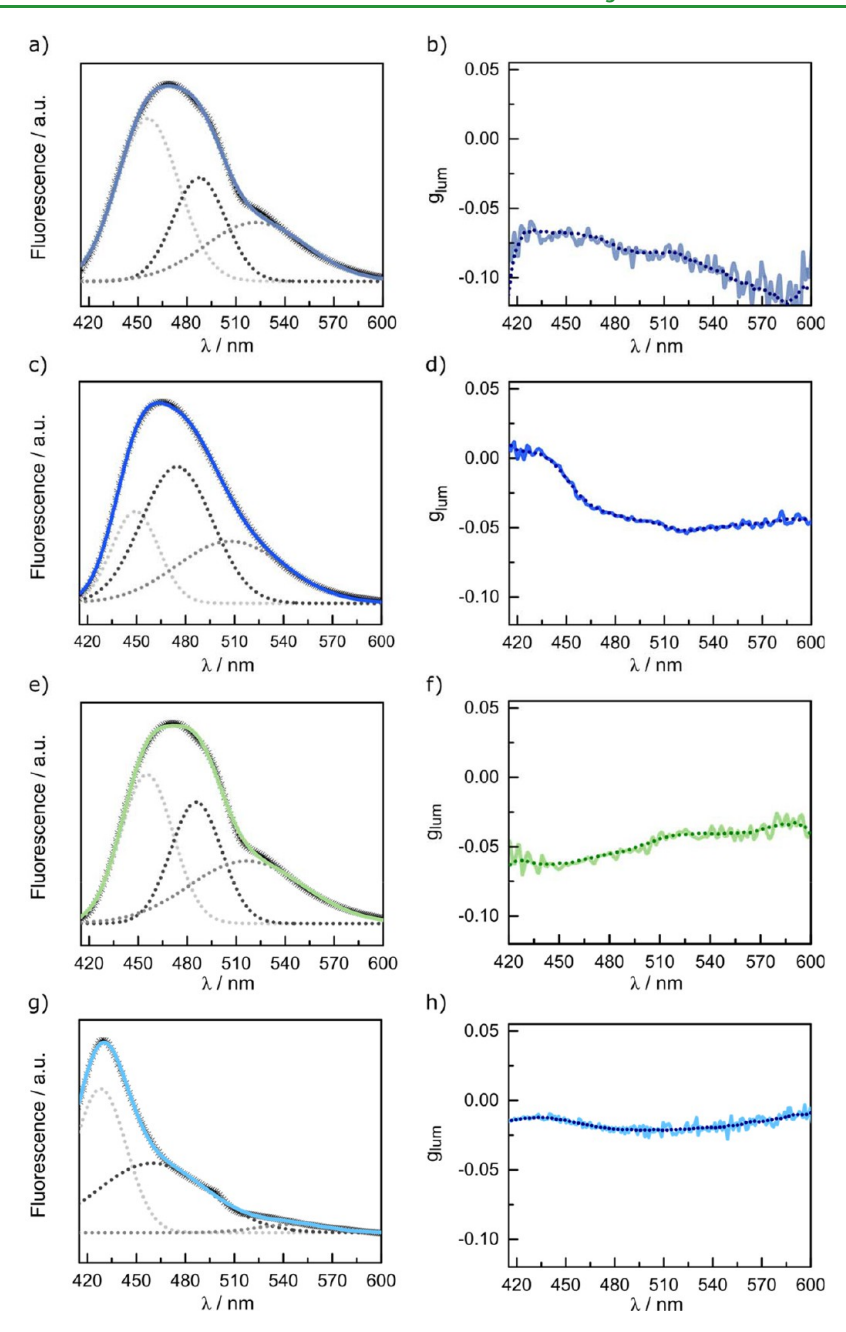


Figure 3. Deconvolution in several Gaussians (in dark and light gray dashed dots) of the emission signal envelope obtained at  $\lambda_{\rm exc}$  = 385 nm (left panel) and  $g_{\rm lum}$  (right panel) vs the wavelengths of: (a, b) BC1 + 0.1 wt % HPS, (c, d) BC3+ 0.1 wt % HPS, (e, f) BC4 + 0.1 wt % HPS, and (g, h) BC5 + 0.1 wt % HPS. Sample thickness: 10  $\mu$ m films sandwiched between untreated quartz substrates after heating to the isotropic liquid phase (T > 170 °C) and subsequent cooling to room temperature ( $T \approx 20$  °C); plots are color-coded based on the morphology color shown in Figure 1. The collective emission as well as the  $|g_{\rm lum}|$  at maximum emission data for the neat B4 templates and the mixtures containing 0.1 wt % HPS are summarized in Table 1. All wavelength-specific  $|g_{\rm lum}|$  data are given in the SI (Table S2).

ing a CPL response. Considering the similar absorption behavior among the B4 templates (Supplementary Information (SI), Figure S1), the vertical electronic transitions from the ground state to the excited states did not depend on the number, position, and relative configuration of the chiral center(s) in the aliphatic side chain(s). The absorption range was between 260 and 420 nm. The emission spectra of BC2, BC3, BC4, and BC5 (BC1 was here excluded because it is the enantiomeric pair of BC2) together with their corresponding CPL spectra are reported in Figure 2. The emission spectrum envelops were all deconvoluted with two Gaussian centered at  $\lambda_1 = 402 \pm 3$  nm and  $\lambda_2 = 444 \pm 3$  nm. The emission decay

profiles of the B4 templates (Table S1 and Figure S2) confirm the expected similar luminescence behavior. These profiles were fitted with three components with an average lifetime value ( $\tau_{\rm av}$ ) in the nanosecond range that corresponds to the fluorescence of the B4 templates. The absolute quantum yield (AQY) was found to be consistent among the B4 templates, with a value of 0.02. However, the generation and magnitude of CPL activity is highly contingent upon the type of B4 morphology. The HNF<sub>mod2</sub> morphologies formed by BC2 and BC3 clearly exhibit higher  $g_{\rm lum}$  values, with the largest average absolute value of  $g_{\rm lum}$  ( $|g_{\rm lum}| = 0.031 \pm 0.005$ ) given by the HNF<sub>mod2a</sub> morphology formed by BC2, which is characterized

Table 1. Summary of Maximum Emission ( $\lambda$ , nm) and  $|g_{lum}|$  Values at Maximum Emission of Neat BC1/BC2-BC5 as Well as of Mixtures of BC1/BC2-BC5 Containing 0.1 wt % HPS

BCLC	BC1/BC2		BC3		BC4		BC5	
morphology HPS (wt %)	$HNF_{mod2a}$	HNF <sub>mod2a</sub>	$HNF_{mod2b}$	HNF <sub>mod2b</sub>	$H\mu F$	HμF 0.1	HLNC	HLNC 0.1
maximum emission( $\lambda$ , nm)	405	469	404	466	402	471	406	430
$ g_{lum} $ at maximum emission	$0.031 \pm 0.005$	$0.07 \pm 0.01$	$0.012 \pm 0.009$	$0.039 \pm 0.001$	$0.027 \pm 0.007$	$0.057 \pm 0.003$	$0.001 \pm 0.007$	$0.018 \pm 0.03$

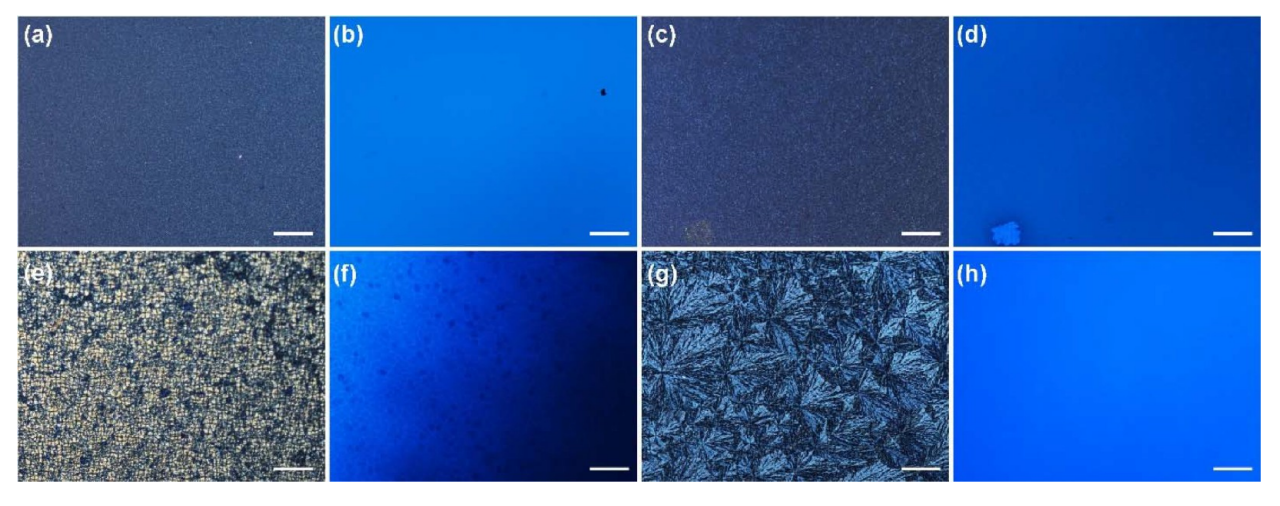


Figure 4. POM images of: (a, b) BC2 + 0.1 wt % HPS without UV and under UV irradiation; (c, d) BC3 + 0.1 wt % HPS without UV and under UV irradiation; (e, f) BC4 + 0.1 wt % HPS after heating to the isotropic liquid phase (T > 160 °C) and subsequent rapid cooling to room temperature ( $T \approx 20$  °C); (g, h) BC5 + 0.1 wt % HPS after heating to the isotropic liquid phase (T > 160 °C) and slow cooling (cooling rate: 5 °C min<sup>-1</sup>) to room temperature ( $T \approx 20$  °C). All scale bars = 100  $\mu$ m.

by a true helical shape with the tightest pitch of p=200 nm in this series (Figure 2a,b). The morphologically related HNF<sub>mod2b</sub> formed by BC3, featuring a longer helical pitch (p=350 nm) gives, as expected, a lower dissymmetry factor, with a recorded average absolute value of  $|g_{\text{lum}}| = 0.012 \pm 0.009$  (Figure 2c,d). The significantly larger H $\mu$ F morphology formed by BC4 delivers an intermediate value of  $|g_{\text{lum}}| = 0.027 \pm 0.007$  (Figure 2e,f). This indicates that within the set of helical BCLC morphologies, size, shape, and the ensuing helical pitch are parameters with underlying trade-offs.

The  $H\mu Fs$  are twisted bands (rather than twisted square rods like the HNFs) and rather more like corkscrews (width and height in Figure 1 refer to the maximum width of height values measured parallel or orthogonal to the layer stacks as they twist). While composed of a quasi-identical number of layers,  $H\mu Fs$  feature notably wider layer stacks than either HNF $_{mod2a}$  or HNF $_{mod2b}$ . Finally, the HLNC morphology formed by BC5 shows practically little to no CPL activity with an average value of  $|g_{lum}| = 0.001 \pm 0.007$  (Figure 2g,h). This is likely the result of the intrinsic heliconical layering, which imposes a cancellation of molecular orientations within each slice of the coaxial layers forming this morphology. These results demonstrate that the regulation of the self-assembly and thus morphology here allows for a modulation and fine-tuning of CPL properties.

The spectrum (based on the AIE) of neat, solid HPS shows a maximum at a wavelength of  $\lambda = 490$  nm in the solid state (thin film with 10  $\mu$ m spacing between quartz substrates prepared by melting HPS and subsequent cooling to room temperature at T = 20 °C). We did not notice any bulk CPL activity ( $g_{\text{lum}} = 0$ ), much in contrast to previous reports for HPS aggregates formed after casting and drying a film from solution. <sup>26</sup> However, some domains show weak positive  $g_{\text{lum}}$ 

and other domains show small negative  $g_{lum}$  values when cast from the melt, as must be expected in the absence of a chiral bias (SI, Figures S3 and S4).

Equipped with such a basic understanding of the CPL properties of neat HPS as well as the four distinct B4 phase morphologies, the next step was to couple the concept of AIE to the intrinsic property of helical nano- and microfilaments to expel guest molecules upon formation on cooling from the isotropic liquid state. Combined, the intrinsic CPL properties of the B4 hosts and the AIE of an expelled helically assembled guest should permit excellent control over and tunable enhancement of the chiroptical properties of these host—guest materials.

Figure 3 and Table 1 summarize the photoluminescence characteristics and the corresponding CPL activity for BC1 (and BC2 with opposite handedness of the template and sign of  $g_{lum}$ ) and BC3-BC5 after the addition of 0.1 wt % HPS after heating these mixtures to the isotropic liquid phase and subsequent cooling to room temperature. The emission signal envelope ( $\lambda_{\text{exc}} = 385 \text{ nm}$ ) can be decomposed into three Gaussians, whose width and intensity largely vary according to the B4 morphology. However, their maximum position centered at 453  $\pm$  4, 481  $\pm$  6, and 515  $\pm$  7 nm are consistently found for the  $HNF_{mod2a/b}$  and  $H\mu F$  morphologies formed by BC1 (BC2), BC3, and BC4, respectively (Figure 3a,c,e). Furthermore, both HNF morphologies generate an enhancement of  $g_{lum}$  with  $|g_{lum}|$  values ranging from 0.05 to 0.1; values that are higher than for any of the neat templates. The B4 morphology strongly alters the wavelength range where the maximum  $|g_{lum}|$  value is detected. While the maximum  $|g_{lum}|$ values of BC1 and BC3, found at 0.085  $\pm$  0.015 and 0.05  $\pm$ 0.001 respectively, were observed at a wavelength of  $\lambda = 515$ nm corresponding to the HPS nano-aggregation, the maximum

 $|g_{lum}|$  value of BC4, at 0.062  $\pm$  0.006, appears in the wavelength range of  $\lambda=[420-453]$  nm, which matches the  $|g_{lum}|$  value reported for the neat compound. The HNF and H $\mu$ F morphologies differ in width, which influences the ratio of aliphatic sublayers vs aromatic ones and therefore the potential for aggregation for HPS molecules. Finally, the BC5 emission signal envelope, BC5 being in the HLNC morphology, appears now as a combination of three Gaussians centered at 428, 460, and 547 nm. This morphology shows some CPL activity after the addition of 0.1 wt % HPS with values of  $|g_{lum}| = 0.018 \pm 0.03$  in the wavelength range of  $\lambda=[450-540]$  nm. These values are considerably smaller than for any of the other B4 morphologies tested here, and the reason lies likely in the structure of the HLNC itself.

HLNCs expose the aliphatic segments of the bent-core molecules because of their coaxial layering. While there is heliconical layering as supported by SEM imaging data, a distinct helical aggregation of HPS that would give rise to a strong CPL signal is here not particularly favorable or likely (Figure 3h). In addition, any kind of energy transfer between the chromophores of BC5 and HPS would be minimized if not suppressed by the exposed sublayers of aliphatic hydrocarbon chains on the outside of the HLNCs, thereby increasing the intermolecular distances between the chromophores. <sup>58</sup>

White-light POM images and the corresponding POM imaging under UV irradiation were carried out for all the mixtures containing 0.1 wt % of HPS (Figure 4 and SI, Figures S5–S8). The uniform luminescent color under irradiation reported in all mixtures suggests a good compatibility between the B4 templates and the HPS dye.

Focusing on the most efficient template, HNF<sub>mod2a</sub> formed by BC1 and BC2, with the highest value(s) of |g<sub>lum</sub>|, another critical question to address is any potential effect of the addition of HPS on the internal structure of the HNF<sub>mod2a</sub> template. If HPS as an AIE guest is expelled by the nanofilaments, the internal structure of the B4 phase should be unaltered. To verify this, small-angle X-ray diffraction (XRD) experiments were carried out for neat BC2 and BC2 + 0.1 wt % HPS. A comparison of the two diffraction patterns confirms that the dual-modulated internal layer structure of the HNFs is intact and unaltered by the addition of HPS as indicated by identical peak positions and intensities (SI, Figure S9). As previously reported for neat BC1 and BC2, 48 neat BC2 and BC2 + 0.1 wt % HPS each show the five identical maxima with  $q_1 = 0.17 \text{ Å}^{-1}$ ,  $q_2 = 0.19 \text{ Å}^{-1}$ ,  $q_3 = 2q_1$ ,  $q_4 = 2q_2$ , and  $q_5 =$ 3q1, indicating an intralayer-modulated structure with a calculated layer spacing of d = 37.25 Å (SI, Figure S9). Unfortunately but inconsequently, the scattering maxima indicating the interlayer dual-modulated layer structure scattering peak at  $q^2 = q_1^2 + q_2^2$  previously seen by synchrotron X-ray diffraction experiments<sup>48</sup> was not resolved with the current laboratory-source X-ray setup. Differential scanning calorimetry (DSC) data further confirm that the thermal properties (specifically the phase transition temperatures and enthalpies) of the B4 templates are unaltered by the addition of HPS (SI, Figure S10).

AlE Studies. To elucidate the expected degree of and contributions from HPS aggregation on these B4 morphology templates, we next investigated the time-dependent fluorescence behavior and recorded the AQY for the B4 templates and the mixtures containing 0.1 wt % HPS. Knowing that the vibrational/torsional motion of the HPS molecule drastically affects the radiative/non-radiative recombination processes of

its excited state, <sup>59,60</sup> emission lifetime data and AQY provide direct evidence of the HPS aggregation. In fact, an enhanced photoluminescence efficiency is traduced by a high AQY value and can be straightforwardly correlated in our case to the restriction of HPS aggregates intramolecular motion.

The fluorescence lifetime data for BC2–BC5 and corresponding mixtures with HPS were obtained by fitting the integrated emission decays according to the following multiexponential model:  $I(t) = \sum_{i=1}^n \alpha_i \exp\left(-\frac{t}{\tau_i}\right)^{61}$  where I(t) is the emission intensity,  $\tau_i$  is the decay time of the i component, and  $\alpha_i$  is its amplitude at t=0. For a single-emitter-containing system, each lifetime component can be assimilated to the emitter being in a different environment or conformation. For a multi-emitter-containing system such as the one considered here, each lifetime component should in principle correspond to one emitter. However, in the solid state, conformational changes due to the AIE effect have also to be considered as well as possible energy transfer between the B4 host and HPS.

First, we will examine mixtures containing 0.1 wt % of HPS as well as neat HPS. Fluorescence lifetime data and AQY of neat HPS and mixtures with 0.1 wt % HPS are reported in Figure 5 and summarized in Table 2. The neat solid-state HPS

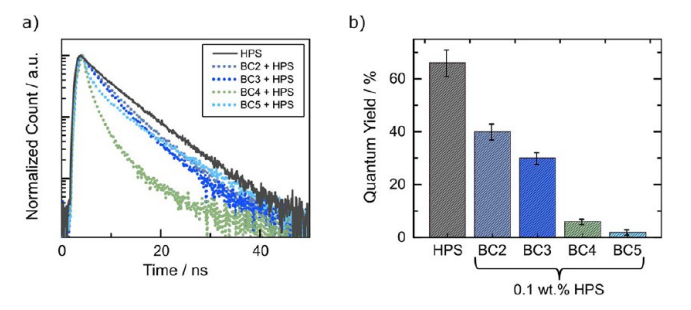


Figure 5. (a) Time-resolved fluorescence and (b) AQY of HPS, BC2 + 0.1 wt % HPS, BC3 + 0.1 wt % HPS, BC4 + 0.1 wt % HPS, and BC5 + 0.1 wt % HPS. Sample thickness: 10  $\mu$ m films sandwiched between untreated quartz substrates after heating to the isotropic liquid phase (T > 170 °C) and subsequent cooling to room temperature ( $T \approx 20$  °C); plots are color-coded based on the morphology color shown in Figure 1. The collective fluorescence lifetime data and AQY of HPS and the mixtures with 0.1 wt % HPS are summarized in Table 2.

emission decay profile was fitted with one component with a lifetime value of 6 ns, which corresponds to its aggregate state with an AQY of 0.66. This emissive component is always present in the BC2-BC5 mixtures. However, the HPS contribution to the overall emission decay varies significantly from one mixture to another, rendering its degree of aggregation within the mixture. For the mixtures BC2 and BC3 containing HPS mixtures, a high contribution of around 60% of the HPS emissive component is calculated together with an additional component. This additional component value is close to the one estimated previously for the neat BC matrices. Such a high contribution for the HPS component is in line with the calculated AQY values. These observations are best explained by the fact that the HNF<sub>mod2a</sub> morphology formed by BC1/BC2 or the HNF<sub>mod2b</sub> morphology formed by BC3 allow for the aggregation and, thus, AIE of HPS along the exposed aromatic sublayer segments. The similar segregation of aromatic guests along exposed aromatic sublayers has

Table 2. Fluorescence Lifetime Data of HPS and the Mixtures Containing 0.1 wt % HPS and BC2 (HNF<sub>mod2a</sub>), BC3 (HNF<sub>mod2b</sub>), BC4 (H $\mu$ F), or BC5 (HLCN)<sup>a</sup>

material	$\tau_1$ (ns)/contribution (%)	$\tau_2$ (ns)/contribution (%)	$\tau_3$ (ns)/contribution (%)	AQY (%)				
HPS	6.0/100			66				
BC2 + 0.1 wt % HPS	6.0/60	2.3/40		40				
BC3 + 0.1 wt % HPS	5.5/56	2.2/44		30				
BC4 + 0.1 wt % HPS	6.7/3	1.9/31	0.5/66	6				
BC5 + 0.1 wt % HPS	6.4/3	1.8/27	0.5/70	2				
<sup>a</sup> The absolute quantum yield (AQY) values are given at $\pm 10\%$ .								

240000 24000 16000 160000 լ-lռ / a.u. 8000 լ-l<sub>R</sub> / a.u. 80000 -8000 -80000 -16000 -160000 -24000 -240000 380 400 420 480 520 600  $\lambda / nm$ 

Figure 6. Plots of the difference between the relative intensity of left- and right-handed CPL,  $I_L - I_R$ , depending on the wavelength,  $\lambda$  (nm), of the neat nanofilament templates (HNF<sub>mod2a</sub>) formed by (a) BC1 (*R-R*) and BC2 (*S-S*) and (b) BC1+ 0.2 wt % HPS and BC2 + 0.2 wt % HPS, each showing significantly larger values than those recorded for the neat templates in (a).

previously been reported for mixtures of HNFs with fullerenes  $^{62,63}$  or nanoparticles decorated with aromatic, promesogenic ligand shells.  $^{64}$ 

Considering the AQY values of 0.4 and 0.3 calculated for BC2 and BC3 mixtures, respectively, the aggregation of HPS appears more efficient in the  $HNF_{mod2a}$  morphology than in the  $HNF_{mod2b}$  one. This can be explained by the smaller dimensions involved in  $HNF_{mod2a}$  with a higher aromatic sublayer surface area by unit volume compared to  $HNF_{mod2b}$ .

The emission decay profiles BC4 and BC5 containing HPS mixtures could only be fitted with three components. The majority one is the shortest one with a lifetime value of 0.5 ns, while the two other components with lifetime values of 6.5 ns (overall contribution: 3%) and 1.8 ns (overall contribution: 30%) correspond to aggregated HPS and the host matrix emission, respectively. This underlines that HPS in this mixture does not aggregate as strongly as in BC1 (or BC2) or BC3. This is further confirmed by the blueshifted emission of the mixture in comparison to the mixtures containing BC1 (or BC2), BC3, or BC4. The H $\mu$ Fs formed by BC4 are formed by helical layers with a larger width ( $w \approx 250-300$  nm) and are overall shaped akin to corkscrews. Hence, by ratio, H $\mu$ Fs expose more aliphatic sublayers at their surface than aromatic ones, which are the regions where HPS would predominantly or favorably aggregate. This effect is further exacerbated by the HLNC morphology formed by BC5. Lack of any exposed aromatic sublayers prevents HPS aggregation and, thus, CPL activity (vide infra).

Increasing the amount of HPS from 0.1 wt % up to 0.4 wt % inevitably leads to HPS aggregation in all mixtures, which goes along with an increase of the AQY values and an increase of the HPS lifetime contribution to the overall emission decays. At 0.4 wt % HPS concentration, only the AIE of HPS is detected, and thus, the emission lifetime decays are fitted with only one component with a lifetime value around 6 ns, close to the one found for neat HPS (SI, Tables S3 and S4 and Figures S11, S12, S15, S16, and S18). We also observe a redshift of the

emission signal, for instance for BC2 + 0.4 wt % HPS compared to the mixtures containing 0.1 and 0.2 wt % HPS (SI, Figures S14 and S15). The deconvolution of the corresponding emission envelope indicates that the two maxima at  $\lambda = 488$  nm and at  $\lambda = 520$  nm correspond to the HPS fluorescence maxima. Hence, at 0.4 wt %, HPS starts to self-aggregate between the nanofilaments, making this concentration the limit in terms of active templating by the B4 morphology. Note that for BC2 + 0.4 wt % HPS, an AQY value of 0.78 was calculated, which is slightly higher than the value found for neat HPS (0.66). Although the accuracy of AQY measurements lies around 10%, such slight increase could also be interpreted as a dilution effect, which minimizes reabsorption phenomena and thus increases the emission efficiency. While there exists an overlap between the emission of BC2 and the absorption of HPS (SI, Figure S13), no energy transfer has been detected between the host and the guest as the lifetime values remain similar when varying the concentration of HPS in the mixture. The self-aggregation of HPS induces the alteration of the  $g_{lum}$  value. The case of selfaggregation in BC2 and BC5 will be discussed later in the manuscript. In BC5 mixture, when doubling the HPS concentration, the  $g_{lum}$  value persists at the same order of magnitude with a reported value at  $g_{lum} = +0.019 \pm 0.05$  when 0.2 wt % of HPS is added. This establishes that the templating is not effective. In consequence, continuing adding HPS in the BC5 mixture gives raise to two regions in the  $g_{lum}$  vs wavelength plot: the [460-540] nm range where the  $g_{lum}$ value for the neat compound is attained ( $g_{lum} = + 0.022 \pm$ 0.005) and the [540–600] nm range where the  $g_{\text{lum}}$  value for HPS is found  $(g_{lum} = +0.02 \pm 0.02)$  (SI, Figure S19).

**Variation of Template Handedness.** A simple and easily accessible way for the given B4 BCLC templates to support the initial assumption that the  $HNF_{mod2a}$  morphologies induce a helical assembly of HPS along the exposed aromatic sublayers is the use of the two  $HNF_{mod2a}$  templates differing in handedness. As reported previously, this was realized by

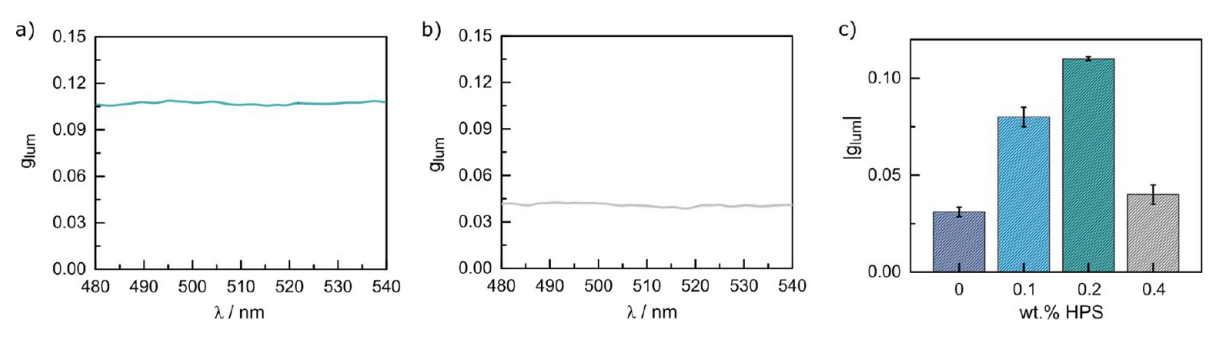


Figure 7. Plots of  $g_{lum}$  vs wavelength ( $\lambda$ , in nm) of BC2 with (a) 0.2 wt % HPS and (b) 0.4 wt % HPS. (c) Overview of the values of  $|g_{lum}|$  depending on the concentration of HPS in the BC2 + HPS mixtures ranging from 0 (neat BC2) to 0.4 wt % HPS.

reversing the configuration of the two chiral centers from p-(R), m-(R) in BC1 to p-(S), m-(S) in BC2. Plots of the difference in intensity between left-handed CPL and right-handed CPL ( $I_{\rm L}-I_{\rm R}$ ) depending on the wavelength of the two neat diastereomers (BC1 vs BC2) indeed show mirror-image plots and maxima at a wavelength of  $\lambda$  = 402 nm (Figure 6a). After the addition of 0.2 wt % HPS in BC1 and BC2, similar mirror-image plots of  $I_{\rm L}-I_{\rm R}$  were observed with maxima at around  $\lambda$  = 480 nm (Figure 6b).

Variation of HPS Concentration: Effects on  $g_{lum}$ . We next studied the most and the least potent HNF<sub>mod2a</sub> and HLNC morphologies in more detail by stepwise doubling the concentration of HPS from 0.1 to 0.4 wt %. As shown in Figures 7a,b, the addition and increase of the concentration of HPS first leads to an almost exponential increase of  $|g_{lum}|$  from  $g_{\text{lum}} = +0.031 \pm 0.005$  for neat BC2 over  $g_{\text{lum}} = +0.08 \pm 0.01$ at 0.1 wt % HPS to  $g_{\text{lum}}$  = + 0.110  $\pm$  0.001 at 0.2 wt % HPS but then to a sudden sharp decrease to  $g_{lum} = +0.040 \pm 0.005$  at 0.4 wt % HPS, which almost returns  $g_{lum}$  to the level of neat BC2 (Figure 7c). The most likely reason is that once HPS has saturated along the aromatic sublayers of the HNF<sub>mod2a</sub>, HPS will begin to self-aggregate between adjacent nanofilaments with this type of more random aggregation leading to lower values of  $g_{\text{lum}}$  on the order of  $10^{-3}$ , potentially canceling out some of the induced dissymmetry created by the supramolecular  $HNF_{mod2a}$  template. The same is true for any possible phase separation of the  $HNF_{mod2a}$  as the concentration of HPS increases beyond a threshold value (here 0.4 wt %). CPL values for aggregated HNFs, as described earlier, are on the order of  $|g_{lum}| \approx 10^{-3}$ . Once self-aggregation among HPS and/or HNF<sub>mod2a</sub> dominates, |g<sub>lum</sub>| will significantly decrease. POM images, recorded with and without UV irradiation, further confirm the self-aggregation once the HPS concentration reaches 0.4 wt % by showing some degree of phase separation between BC2 and HPS (SI, Figure S20). The maximum emission wavelength in the fluorescence spectrum of BC2 + 0.4 wt % HPS (SI, Figures S14 and S15) approaches the maximum emission wavelength seen in the fluorescence spectra of neat HPS and no additional maxima. The same occurs for BC5 + 0.4 wt % HPS (SI, Table S3 and Figures S16 and S17). Doubling the concentration of HPS from 0.2 to 0.4 wt % in BC5 does not lead to an observable change in |g<sub>lum</sub>| (SI, Figure S19) compared to the  $|g_{lum}|$  of BC5 + 0.1 wt % HPS as discussed earlier. This confirms the hypothesis reached after evaluating the fluorescence decay times, that is, that the HLNC morphology lacks exposed aromatic sublayers, which prevents HPS aggregation, thereby resulting in the lowest CPL activity. TEM images of BC2 + 0.2 wt % HPS as well as BC5 + 0.2 wt % HPS show the morphology of the two BCLC templates but

no detectable signature of HPS aggregation at this magnification (SI, Figures S21 and S22, respectively), indicating that HPS does not visibly (at TEM magnification) phase-separate. Further evidence to help explain the different mechanisms for nano- and microfilaments with respect to the HLNCs at a constant concentration of HPS are the luminescence spectra themselves. For the former the samples emit bright turquoise light under  $\lambda_{\rm exc}$  = 365 nm irradiation (SI, Figure S23a,b), while for the latter, the fluorescence could hardly be detected even under identical irradiation conditions (SI, Figure S23c). While not detectable by the TEM imaging, the collective data do support the argument that HPS does more favorably aggregate on template filaments with exposed aromatic sublayers and not on HLNCs featuring an entirely aliphatic interface.

**Second-Level Templating Using Confinement in Nanopores.** A rather versatile approach to template-assisted self-assembly of soft-matter nanostructures is the confinement in nanochannels of anodic aluminum oxide (AAO) films serving as tunable nanoporous media. <sup>65–68</sup> The dependence of the HNF internal structure and external morphology (shape and pitch) on AAO pore size was extensively studied by Yoon et al. This work established the dependency of the AAO pore diameter on the morphology of nanoconfined HNFs, whereby one nanochannel can accommodate one HNF if 0.7  $w_{\text{bulk}} < \omega_{\text{AAO}} < 2 w_{\text{bulk}}$ , where  $\omega_{\text{AAO}}$  is the AAO pore diameter and  $w_{\text{bulk}}$  is the width of the unconfined HNFs in the bulk. <sup>69–71</sup> The width of the HNFs used in our experiments is  $w_{\text{bulk}} \approx 40$  nm, and the diameter of AAO is  $\omega_{\text{AAO}} = 60$  nm, (SI, Figure S24) following this established principle.

The sample preparation is quite significant when confining HNFs in AAO pores. In practice, the mixture of BC1 + 0.2 wt % HPS was placed on the top of the AAO film rested on a hot stage to generate a temperature gradient parallel to the pore direction, with the lowest temperature at the top of the AAO film. As soon as the temperature reaches the clearing point of BC1 ( $T_{\rm cl}$  = 190 °C), the mixture is sucked into the AAO pores by capillary force. By slowly decreasing the temperature at a cooling rate of 5 °C min<sup>-1</sup> to eliminate the effect of nucleation, the residual bulk material at the surface of the AAO wafer was continuously removed over three heating/cooling cycles. Subsequently, nucleation of the HNFs within the AAO pores appears in each individual AAO pore during such heating/cooling cycle, similarly with the added HPS (Figure 8).

For neat BC1 confined in 60 nm AAO pores, a  $|g_{lum}|$  value of 0.08  $\pm$  0.003 was found—an increase from  $|g_{lum}| \approx 0.031 \pm 0.005$  in the absence of AAO confinement (Figure 9a). At 0.1 wt % HPS in BC1 under confinement, the  $|g_{lum}|$  increases from 0.085  $\pm$  0.015 to 0.10  $\pm$  0.02 in the [480–540] nm range (Figure 9b). This value further increases to  $|g_{lum}| = 0.25 \pm 0.03$ 

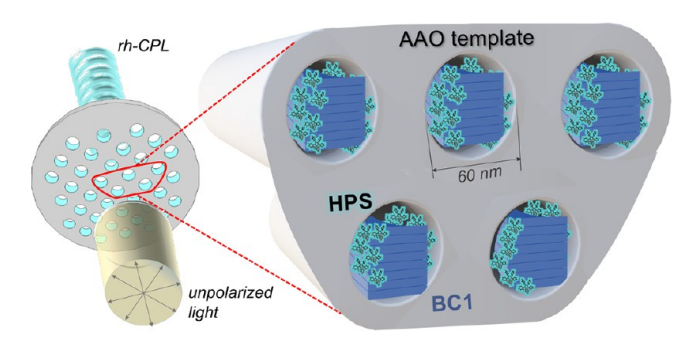


**Figure 8.** Schematic drawing demonstrating the confinement of right-handed HNF<sub>mod2a</sub> formed by BC1 after the addition of HPS in the pores of AAO with an inner diameter of  $\varnothing_{AAO} = 60$  nm during the CPL measurement with the pores along the irradiation path.

when the concentration of HPS is raised to 0.2 wt % (Figure 9c); thus, an about 3-fold increase is achieved compared to neat BC1 confined in AAO.

There are two main reasons for this observation: first, all HNF $_{\rm mod2a}$  are aligned in the same direction when confined within the parallel nanopores. This directionality alone results in a larger CPL efficiency compared to the randomly aligned HNFs without confinement. Second, the excess space in the nanopores along the helical grooves induces a change of the HNF structure such that it enables each single nanofilament confined within the nanopore to fill that space more efficiently. Because of this morphological change, the helical pitch, p, of the HNF $_{\rm mod2a}$  tightens from p=200 nm to a value of  $p\approx 130$  nm. Earlier experiments demonstrated that increasing the concentration of a chiral guest (i.e., an axially chiral binaphthyl derivative) leads to a gradual reduction of p when HNFs are

confined in 60 nm AAO channels. She While the HNF  $_{\rm mod2a}$  are crystalline structures, the mixtures with HPS are prepared in the melt, where the molecular homochirality of BC1 could favor one handedness of the propeller-like structure of HPS over the other. In such scenario, HPS would serve as a chiral (non-racemic) additive inducing a tighter value of p, just as in the case of the binaphthyl derivatives. Thus, a combination of a lower value of p (here reduced by 35%) and more efficient localized heliconical HPS aggregation within the confinement of these nanopores facilitates the higher values for  $|g_{\rm lum}|$  again until an HPS concentration of 0.2 wt % is reached.

Analogously to the non-confined case, however, the concentration of HPS in BC1 is limited to concentrations lower than 0.4 wt %, where the value of  $|g_{lum}|$  decreases back to  $|g_{lum}| = 0.13 \pm 0.02$  (Figure 9d). The bar diagram in Figure 9e illustrates the same trend already shown for the non-confined case. Initially, increasing the concentration of HPS in BC1 leads to an exponential increase in  $|g_{lum}|$  up to a concentration of HPS of about 0.2 wt % and then drops off again once the concentration is doubled to 0.4 wt %. However, confinement, as predicted, leads to higher values for  $|g_{lum}|$ . Scanning electron microscopy (SEM) images confirm the confinement of single HNF<sub>mod2a</sub> within each of the 60 nm AAO nanopores (Figure 9f and SI, Figure S25).

Structural Color + AIE as a Potential Anti-Counterfeiting or Rate-of-Temperature Change Indicator Solution. Finally, we believe that the variation in wavelength of the displayed structural colors of the templating B4 morphologies (as shown in Figure 1) coupled with the AIE of HPS can be used in a patterning strategy for an optical rate-of-temperature change indicator or as an anti-counterfeiting solution. Recent work by Yoon and coworkers has shown that

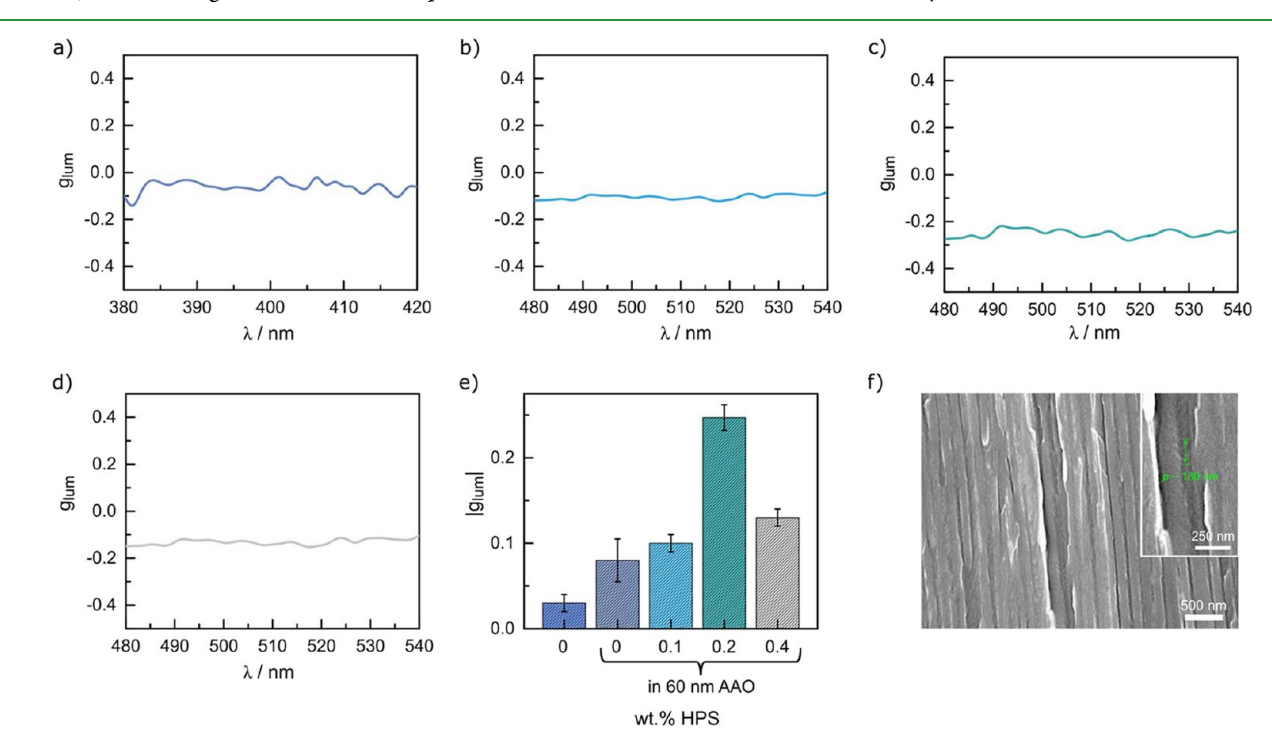


Figure 9. (a–d) Plots of  $g_{lum}$  vs wavelength (λ, in nm) of BC1 confined in 60 nm AAO nanopores: (a) neat BC1 in the [380–420] nm range where the emission is maximal, (b) BC1 + 0.1 wt % HPS, (c) BC1 + 0.2 wt % HPS, and (d) BC1 + 0.4 wt % HPS in the [480–540] nm range where the emission is maximal. (e) Summary of  $|g_{lum}|$  vs concentration of HPS from 0 to 0.4 wt % in BC1 under AAO confinement. (f) SEM image of BC1 + 0.2 wt % HPS confined in 60 nm AAO nanopores, showing the confinement of single HNF<sub>mod2a</sub> (with BC1 forming right-handed HNF<sub>mod2a</sub> as in the absence of HPS).

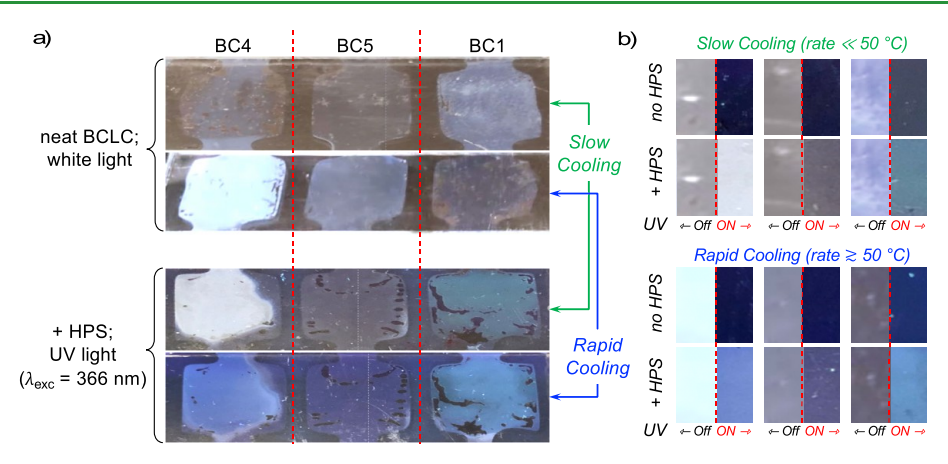


Figure 10. (a) Photographs of cells (cell gap = 5 μm) filled with BC1, BC4, and BC5 after heating to the isotropic liquid phase of all compounds and observed after slow cooling ( $\sim$ 5 °C min<sup>-1</sup>) or rapid cooling to room temperature ( $\sim$  50 °C min<sup>-1</sup>, i.e., thermally quenched): (top rows, without HPS as seen under white light; bottom rows, with 0.2 wt % HPS under UV irradiation at  $\lambda_{\rm exc}$  = 365 nm). (b) Images showing a possible resulting color pattern composed of structural color (UV OFF) and AIE (with UV ON).

the structural color of azobenzene-based BLCLs can be used for dynamic color reflectors. In this context, the unique phase behavior of and polymorphism displayed by BC4 and the biphasic behavior found for BC5 could be exploited in an indicator that could visually show and distinguish between slow and rapid temperature changes from temperatures around 250 °C (decomposition temperature of the BCLC molecules) to and well below room temperature since these B4 morphologies form stable glassy states as most other B4 filament phases (as shown earlier by differential scanning calorimetry experiments). The addition of HPS also provides the ability to create tamper-proof, unique labels or tags for anti-counterfeiting applications using a combination of structural and AIE photoluminescence colors. This concept is visualized in Figure 10.

Figure 10a shows photographs of ternary cells (cell gap = 5  $\mu$ m) filled with either BC1, BC4, or BC5. The top two rows show each compound under white light illumination after heating to the isotropic liquid phase and subsequent cooling down to room temperature (~20 °C) at either a slow or rapid cooling rate. Particularly obvious is the color difference observed for BC4 depending on the cooling rate since BC4 forms a B4 morphology (here H $\mu$ F) only upon rapid cooling but not upon slow cooling. In contrast, the relatively low intensity of the structural color displayed by BC1 (HNF<sub>mod2a</sub> morphology) changes only insignificantly. For BC5, however, the biphasic regime with B1/B4 phase coexistence<sup>50</sup> gives rise to a more intense blue structural color upon rapid cooling.

To further enhance the complexity, adding 0.2 wt % of HPS (emission:  $\lambda_{\rm max}$  = 498 nm) leads to another color pattern under UV irradiation ( $\lambda_{\rm exc}$  = 365 nm). The two bottom rows in Figure 7a demonstrate the different degree of how the B1 (here the Col<sub>ob</sub> – p2/m formed by BC4 upon slow cooling) and the B4 morphologies expel HPS. For BC4, only the B4 H $\mu$ F expels HPS; the Col<sub>ob</sub> phase formed upon slow cooling does not, thereby not leading to AIE. For BC5, the HLNC morphology does not show significant aggregation of HPS, and therefore, virtually no AIE is observed as seen in the CPL measurements described earlier. As expected, BC1 forming HNF<sub>mod2a</sub> expels HPS, and depending on the cooling rate, different AIE wavelengths are observed that appear to capture different degrees of HPS aggregation.

This eventually leads to the quite complex blueish color pattern shown in Figure 10b depending on whether a color (or compound) pixel is doped with HPS or not as well as whether UV irradiation is applied or not. Keeping in mind that all BCLC molecules have the exact identical molecular weight, only more advanced chemical analyses (not even that straightforward using <sup>1</sup>H NMR) would allow anyone to break the embedded code of these anti-counterfeiting  $^{73-75}$  or temperature-rate indicator devices. An added advantage provided by these materials and for the ensuing potential anti-counterfeiting tags or temperature-rate indicators is the glassy state attained at room temperature. <sup>48–50,76</sup> Patterning by printing or plotting would make these indicators or tags easy to produce as well as easily randomized for additional security, practically impossible to break if coded. Furthermore, residing within one, here blue, color palette also eliminates concerns for potential observers with color vision deficiencies.

# CONCLUSIONS

In this work, a strategy for generating tunable CPL materials from supramolecular chiral assemblies based on bent-core liquid crystals forming various B4 phase helical (heliconical) nano- or microfilament templates is presented. The intrinsic geometric differences among the B4 templates, such as overall dimensions (width, height, and helical pitch) and the ensuing differences in the degree of exposed aromatic segments or sublayers, ultimately leads to varying degrees of CPL activity as indicated by the values of  $|g_{lum}|$ . The evidence obtained from these experiments strongly supported the restricted intramolecular rotation model for the AIE HPS molecules within the B4 templates. As predicted a priori, the smallest of the B4 templates with the largest overall area fraction of exposed aromatic sublayers, where HPS will tend to aggregate, the HNF<sub>mod2a</sub>, shows the highest efficiency for CPL. The coassembly of the nano- or microfilaments with HPS allows for a tuning of the CPL intensity as well as wavelength maximum from about 420 to 520 nm when illuminated by a  $\lambda_{\rm exc}$  = 385 nm light source, while adding only a small amount of HPS with the highest efficiency recorded at 0.2 wt %. In contrast to other reports on the origin of CPL of HPS in the solid state, those of the B4 hosts that actively generate the CPL of HPS facilitate a heliconical chiral assembly of HPS directed by their exposed aromatic sublayers, which dictate magnitude as well as

handedness. Furthermore, the confinement of the most efficient  $HNF_{mod2a}$  template formed by BC1 (or BC2 with opposite handedness but identical magnitude) in 60 nm AAO provides an opportunity to further enhance the |glum| up to a value of 0.25 by facilitating parallel alignment of the HNF<sub>mod2a</sub> supramolecular architectures with a reduced helical pitch parallel to the excitation source. Such approach provides a pathway to tune CPL, ultimately leading to an about 8-fold increase of  $|g_{lum}|$  from neat BC1 to BC1 + 0.2 wt % HPS in 60 nm AAO with an additional enhancement possible using a homochiral AIE dye that would reduce the helical pitch under confinement as shown in earlier work.<sup>56</sup> Finally, the combination of structural color exhibited by all the B4 templates with the AIE inherent to the dye used, HPS, was demonstrated as a potential avenue for applications as temperature-rate detection or anti-counterfeiting tags.

# ASSOCIATED CONTENT

# Supporting Information

The Supporting Information is available free of charge at https://pubs.acs.org/doi/10.1021/acsami.2c05012.

> Additional UV-Vis and fluorescence spectra; timeresolved fluorescence decay; CPL and absolute quantum yield data; SEM and TEM images; POM photomicrographs with and without UV irradiation; sample photographs under UV irradiation; XRD data (PDF)

#### AUTHOR INFORMATION

### **Corresponding Authors**

Marianne E. Prévôt – Advanced Materials and Liquid Crystal Institute, Kent State University, Kent, Ohio 44242-0001, United States; Email: mprevot1@kent.edu

Torsten Hegmann - Materials Science Graduate Program, Advanced Materials and Liquid Crystal Institute, Department of Chemistry and Biochemistry, and Brain Health Research Institute, Kent State University, Kent, Ohio 44242-0001, United States; o orcid.org/0000-0002-6664-6598; Phone: +1 (330) 672-7770; Email: thegmann@ kent.edu

### **Authors**

Jiao Liu – Materials Science Graduate Program and Advanced Materials and Liquid Crystal Institute, Kent State University, Kent, Ohio 44242-0001, United States

Yann Molard - Univ Rennes, ISCR - UMR 6226, F-35000 Rennes, France; orcid.org/0000-0002-6295-0883

Complete contact information is available at: https://pubs.acs.org/10.1021/acsami.2c05012

#### **Author Contributions**

J.L. performed the sample preparation, SEM and TEM imaging, as well as the UV-Vis measurements. J.L., Y.M., and M.E.P. performed the CPL measurements and POM imaging. M.E.P. and Y.M. performed the fluorescence lifetime measurements. J.L., Y. M., M.E.P., and T.H. performed the data analysis, and all authors co-wrote the manuscript. T.H. directed the study.

#### **Funding**

The work was financially supported by the US National Science Foundation (NSF, DMR-1506018 and DMR-1904091), the Ohio Third Frontier program for Ohio Research Scholars "Research Cluster on Surfaces in Advanced

Materials", which also supports the Materials Characterization and Imaging facility at the Advanced Materials and Liquid Crystal Institute (KSU), where some of the current SEM and TEM data were acquired.

#### Notes

The authors declare no competing financial interest.

#### **ACKNOWLEDGMENTS**

We acknowledge Dr. Guiseppe Strangi and Andrew Lininger for access to and help with some preliminary time-resolved fluorescence lifetime measurements at Case Western Reserve University. We also acknowledge Dr. Gregory Taupier for help with the fluorescence lifetime and absolute quantum yield measurements at Caphter Platform from UAR ScanMAT. The authors acknowledge access to the X-ray scattering facility at the Advanced Materials and Liquid Crystal Institute (AMLCI) at Kent State University, which was financially supported by the National Science Foundation (DMR-2017845), the State of Ohio (The Ohio Department of Higher Education Action Fund), and Kent State University.

# ABBREVIATIONS

AAO, anodic aluminum oxide ACQ, aggregation-caused quenching AIE, aggregation-induced emission AQY, absolute quantum yield BCLC, bent-core liquid crystal CD, circular dichroism CPL, circular polarized luminescence HLNC, heliconical-layered nanocylinders  $H\mu F$ , helical microfilament HNF, helical nanofilament HPS, 1,1,2,3,4,5-hexaphenyl-1*H*-silole LC, liquid crystal POM, polarized optical microscopy SEM, scanning electron microscopy TEM, transmission electron microscopy UV, ultraviolet XRD, X-ray diffraction

#### REFERENCES

- (1) Ariga, K.; Mori, T.; Kitao, T.; Uemura, T. Supramolecular Chiral Nanoarchitectonics. Adv. Mater. 2020, 32, 1905657.
- (2) Kelvin, W. T. Baltimore Lectures on Molecular Dynamics and the Wave Theory of Light. C. J. Clay and Sons: London, 1904.
- (3) Barron, L. D. From Cosmic Chirality to Protein Structure and Function: Lord Kelvin's Legacy. Chirality 2012, 24, 879-893.
- (4) Mateos-Timoneda, M. A.; Crego-Calama, M.; Reinhoudt, D. N. Supramolecular Chirality of Self-Assembled Systems in Solution. Chem. Soc. Rev. 2004, 33, 363-372.
- (5) Kawasaki, T.; Matsumura, Y.; Tsutsumi, T.; Suzuki, K.; Ito, M.; Soai, K. Asymmetric Autocatalysis Triggered by Carbon Isotope (C-13/C-12) Chirality. Science 2009, 324, 492-495.
- (6) Wang, M.; Zhou, P.; Wang, J. Q.; Zhao, Y. R.; Ma, H. C.; Lu, J. R.; Xu, H. Left or Right: How Does Amino Acid Chirality Affect the Handedness of Nanostructures Self-Assembled from Short Amphiphilic Peptides? J. Am. Chem. Soc. 2017, 139, 4185-4194.
- (7) Blackmond, D. G. Autocatalytic Models for the Origin of Biological Homochirality. Chem. Rev. 2020, 120, 4831-4847.
- (8) Kim, Y.; Yeom, B.; Arteaga, O.; Yoo, S. J.; Lee, S. G.; Kim, J. G.; Kotov, N. A. Reconfigurable Chiroptical Nanocomposites with Chirality Transfer from the Macro- to the Nanoscale. Nat. Mater. **2016**, *15*, 461–468.

- (9) Albano, G.; Pescitelli, G.; Di Bari, L. Chiroptical Properties in Thin Films of  $\pi$ -Conjugated Systems. *Chem. Rev.* **2020**, 120, 10145–10243.
- (10) Mun, J.; Kim, M.; Yang, Y.; Badloe, T.; Ni, J. C.; Chen, Y.; Qiu, C. W.; Rho, J. Electromagnetic Chirality: From Fundamentals to Nontraditional Chiroptical Phenomena. *Light-Sci. Appl.* **2020**, *9*, 139.
- (11) Verreault, D.; Moreno, K.; Merlet, E.; Adamietz, F.; Kauffmann, B.; Ferrand, Y.; Olivier, C.; Rodriguez, V. Hyper-Rayleigh Scattering as a New Chiroptical Method: Uncovering the Nonlinear Optical Activity of Aromatic Oligoamide Foldamers. *J. Am. Chem. Soc.* **2020**, 142, 257–263.
- (12) Berova, N.; Nakanishi, K. Exciton Chirality Method: Principles and Applications, In *Circular Dichroism. Principles and Applications 2nd Edition*, Berova, N.; Nakanishi, K.; Woody, R. (Eds.), 2000. pp. 337—382 (Wiley, 2000).
- (13) Andrews, S. S.; Tretton, J. Physical Principles of Circular Dichroism. J. Chem. Educ. 2020, 97, 4370-4376.
- (14) Sang, Y. T.; Han, J. L.; Zhao, T. H.; Duan, P. F.; Liu, M. H. Circularly Polarized Luminescence in Nanoassemblies: Generation, Amplification, and Application. *Adv. Mater.* **2020**, *32*, 1900110.
- (15) Kumar, J.; Nakashima, T.; Kawai, T. Circularly Polarized Luminescence in Chiral Molecules and Supramolecular Assemblies. *J. Phys. Chem. Lett.* **2015**, *6*, 3445–3452.
- (16) Li, H. K.; Cheng, J.; Zhao, Y. H.; Lam, J. W. Y.; Wong, K. S.; Wu, H. K.; Li, B. S.; Tang, B. Z. L-Valine Methyl Ester-Containing Tetraphenylethene: Aggregation-Induced Emission, Aggregation-Induced Circular Dichroism, Circularly Polarized Luminescence, and Helical Self-Assembly. *Mater. Horiz.* 2014, 1, 518–521.
- (17) Li, J. F.; Hou, C. X.; Huang, C.; Xu, S. Q.; Peng, X. L.; Qi, Q.; Lai, W. Y.; Huang, W. Boosting Circularly Polarized Luminescence of Organic Conjugated Systems via Twisted Intramolecular Charge Transfer. *Res. China* **2020**, *2020*, 3839160.
- (18) Liu, J. Z.; Su, H. M.; Meng, L. M.; Zhao, Y. H.; Deng, C. M.; Ng, J. C. Y.; Lu, P.; Faisal, M.; Lam, J. W. Y.; Huang, X. H.; Wu, H. K.; Wong, K. S.; Tang, B. Z. What Makes Efficient Circularly Polarised Luminescence in the Condensed Phase: Aggregation-Induced Circular Dichroism and Light Emission. *Chem. Sci.* **2012**, *3*, 2737–2747.
- (19) Luo, Z. W.; Tao, L.; Zhong, C. L.; Li, Z. X.; Lan, K.; Feng, Y.; Wang, P.; Xie, H. L. High-Efficiency Circularly Polarized Luminescence from Chiral Luminescent Liquid Crystalline Polymers with Aggregation-Induced Emission Properties. *Macromolecules* **2020**, 53, 9758–9768.
- (20) Tohgha, U.; Deol, K. K.; Porter, A. G.; Bartko, S. G.; Choi, J. K.; Leonard, B. M.; Varga, K.; Kubelka, J.; Muller, G.; Balaz, M. Ligand Induced Circular Dichroism and Circularly Polarized Luminescence in CdSe Quantum Dots. ACS Nano 2013, 7, 11094–11102
- (21) Lin, J. T.; Chen, D. G.; Yang, L. S.; Lin, T. C.; Liu, Y. H.; Chao, Y. C.; Chou, P. T.; Chiu, C. W. Tuning the Circular Dichroism and Circular Polarized Luminescence Intensities of Chiral 2D Hybrid Organic-Inorganic Perovskites through Halogenation of the Organic Ions. *Angew. Chem., Int. Ed.* **2021**, *60*, 21434–21440.
- (22) Tanaka, H.; Inoue, Y.; Mori, T. Circularly Polarized Luminescence and Circular Dichroisms in Small Organic Molecules: Correlation between Excitation and Emission Dissymmetry Factors. *ChemPhotoChem* **2018**, *2*, 386–402.
- (23) Anetai, H.; Takeda, T.; Hoshino, N.; Arak, Y.; Wada, T.; Yamamoto, S.; Mitsuishi, M.; Tsuchida, H.; Ogoshi, T.; Akutagawa, T. Circular Polarized Luminescence of Hydrogen-Bonded Molecular Assemblies of Chiral Pyrene Derivatives. *J. Phys. Chem. C* **2018**, *122*, 6323–6331.
- (24) Dang, Y. Y.; Liu, X. L.; Sun, Y. J.; Song, J. W.; Hu, W. P.; Tao, X. T. Bulk Chiral Halide Perovskite Single Crystals for Active Circular Dichroism and Circularly Polarized Luminescence. *J. Phys. Chem. Lett.* **2020**, *11*, 1689–1696.
- (25) Tan, Y. B.; Okayasu, Y.; Katao, S.; Nishikawa, Y.; Asanoma, F.; Yamada, M.; Yuasa, J.; Kawai, T. Visible Circularly Polarized

- Luminescence of Octanuclear Circular Eu(III) Helicate. J. Am. Chem. Soc. 2020, 142, 17653–17661.
- (26) Xue, S.; Meng, L. M.; Wen, R. S.; Shi, L.; Lam, J. W.; Tang, Z. Y.; Li, B. S.; Tang, B. Z. Unexpected Aggregation Induced Circular Dichroism, Circular Polarized Luminescence and Helical Assembly from Achiral Hexaphenylsilole (HPS). RSC Adv. 2017, 7, 24841–24847.
- (27) Ma, K.; Chen, W. J.; Jiao, T. F.; Jin, X.; Sang, Y. T.; Yang, D.; Zhou, J.; Liu, M. H.; Duan, P. F. Boosting the Circularly Polarized Luminescence of Small Organic Molecules via Multi-Dimensional Morphology Control. *Chem. Sci.* **2019**, *10*, 6821–6827.
- (28) Li, X. J.; Hu, W. R.; Wang, Y. X.; Quan, Y. W.; Cheng, Y. X. Strong CPL of Achiral AIE-Active Dyes Induced by Supramolecular Self-Assembly in Chiral Nematic Liquid Crystals (AIE-N\*-LCs). Chem. Commun. 2019, 55, 5179–5182.
- (29) Li, X. J.; Li, Q.; Wang, Y. X.; Quan, Y. W.; Chen, D. Z.; Cheng, Y. X. Strong Aggregation-Induced CPL Response Promoted by Chiral Emissive Nematic Liquid Crystals (N\*-LCs). *Chem.-Eur. J.* **2018**, 24, 12607–12612.
- (30) Luo, J. D.; Xie, Z. L.; Lam, J. W. Y.; Cheng, L.; Chen, H. Y.; Qiu, C. F.; Kwok, H. S.; Zhan, X. W.; Liu, Y. Q.; Zhu, D. B.; Tang, B. Z. Aggregation-Induced Emission of 1-Methyl-1,2,3,4,5-pentaphenyl-silole. *Chem. Commun.* **2001**, *18*, 1740–1741.
- (31) Zhao, Z. J.; He, B. R.; Tang, B. Aggregation-Induced Emission Of Siloles. *Chem. Sci.* **2015**, *6*, 5347–5365.
- (32) Hong, Y. N.; Lam, J. W. Y.; Tang, B. Z. Aggregation-Induced Emission: Phenomenon, Mechanism and Applications. *Chem. Commun.* **2009**, 29, 4332–4353.
- (33) Song, F. Y.; Zhao, Z.; Liu, Z. Y.; Lam, J. W. Y.; Tang, B. Z. Circularly Polarized Luminescence from AIEgens. *J. Mater. Chem. C* **2020**, *8*, 3284–3301.
- (34) Song, F. Y.; Cheng, Y. H.; Liu, Q. M.; Qiu, Z. J.; Lam, J. W. Y.; Lin, L. B.; Yang, F. F.; Tang, B. Z. Tunable Circularly Polarized Luminescence from Molecular Assemblies of Chiral AlEgens. *Mater. Chem. Front.* **2019**, *3*, 1768–1778.
- (35) Feng, H. T.; Lam, J. W. Y.; Tang, B. Z. Self-Assembly of AIEgens. Coordin. Chem. Rev. 2020, 406, No. 213142.
- (36) Zhang, W. N.; Chang, H.; Ai, J.; Che, S. A.; Duan, Y. Y.; Han, L. Spontaneous Chiral Self-Assembly of Achiral AIEgens into AIEgen-Silica Hybrid Nanotubes. *Chem. Commun.* **2019**, *55*, 14438–14441.
- (37) Zhang, S. W.; Fan, J.; Wang, Y. X.; Li, D.; Jia, X. D.; Yuan, Y.; Cheng, Y. X. Tunable Aggregation-Induced Circularly Polarized Luminescence of Chiral AIEgens via the Regulation of Mono-/Di-Substituents of Molecules or Nanostructures of Self-Assemblies. *Mater. Chem. Front.* **2019**, *3*, 2066–2071.
- (38) Feng, H. T.; Gu, X. G.; Lam, J. W. Y.; Zheng, Y. S.; Tang, B. Z. Design of Multi-Functional AIEgens: Tunable Emission, Circularly Polarized Luminescence and Self-Assembly by Dark Through-Bond Energy Transfer. *J. Mater. Chem. C* **2018**, *6*, 8934–8940.
- (39) Han, J. Q.; Li, Y. P.; Yuan, J.; Li, Z. F.; Zhao, R. X.; Han, T. Y.; Han, T. D. To direct the Self-Assembly of AIEgens by Three-Gear Switch: Morphology Study, Amine Sensing and Assessment of Meat Spoilage. Sens. Actuators, B 2018, 258, 373–380.
- (40) Chen, B.; Nie, H.; Lu, P.; Zhou, J.; Qin, A. J.; Qiu, H. Y.; Zhao, Z. J.; Tang, B. Z. Conjugation Versus Rotation: Good Conjugation Weakens the Aggregation-Induced Emission Effect of Siloles. *Chem. Commun.* **2014**, *50*, 4500–4503.
- (41) Mullin, J. L.; Tracy, H. J.; Ford, J. R.; Keenan, S. R.; Fridman, F. Characteristics of Aggregation Induced Emission in 1,1-Dimethyl-2,3,4,5-tetraphenyl and 1,1,2,3,4,5-Hexaphenyl Siloles And Germoles. *J. Inorg. Organomet. Polym. Mater.* **2007**, *17*, 201–213.
- (42) Shi, Y. H.; Duan, P. F.; Huo, S. W.; Li, Y. G.; Liu, M. H. Endowing Perovskite Nanocrystals with Circularly Polarized Luminescence. *Adv. Mater.* **2018**, *30*, 1705011.
- (43) Huo, S. W.; Duan, P. F.; Jiao, T. F.; Peng, Q. M.; Liu, M. H. Self-Assembled Luminescent Quantum Dots To Generate Full-Color and White Circularly Polarized Light. *Angew. Chem., Int. Ed.* **2017**, *56*, 12174–12178.

- (44) Xing, P. Y.; Zhao, Y. L. Controlling Supramolecular Chirality in Multicomponent Self-Assembled Systems. *Acc. Chem. Res.* **2018**, *51*, 2324–2334
- (45) Goto, T.; Okazaki, Y.; Ueki, M.; Kuwahara, Y.; Takafuji, M.; Oda, R.; Ihara, H. Induction of Strong and Tunable Circularly Polarized Luminescence of Nonchiral, Nonmetal, Low-Molecular-Weight Fluorophores Using Chiral Nanotemplates. *Angew. Chem., Int. Ed.* **2017**, *56*, 2989–2993.
- (46) Sugimoto, M.; Liu, X. L.; Tsunega, S.; Nakajima, E.; Abe, S.; Nakashima, T.; Kawai, T.; Jin, R. H. Circularly Polarized Luminescence from Inorganic Materials: Encapsulating Guest Lanthanide Oxides in Chiral Silica Hosts. *Chem.-Eur. J.* **2018**, 24, 6519–6524.
- (47) Han, J.; You, J.; Li, X.; Duan, P.; Liu, M. Full-Color Tunable Circularly Polarized Luminescent Nanoassemblies of Achiral AIEgens in Confined Chiral Nanotubes. *Adv. Mater.* **2017**, *29*, 1606503.
- (48) Li, L.; Salamonczyk, M.; Jákli, A.; Hegmann, T. A Dual Modulated Homochiral Helical Nanofilament Phase with Local Columnar Ordering Formed by Bent Core Liquid Crystals: Effects of Molecular Chirality. *Small* **2016**, *12*, 3944–3955.
- (49) Li, L.; Salamonczyk, M.; Shadpour, S.; Zhu, C. H.; Jákli, A.; Hegmann, T. An Unusual Type of Polymorphism in a Liquid Crystal. *Nat. Commun.* **2018**, *9*, 714.
- (50) Shadpour, S.; Nemati, A.; Boyd, N. J.; Li, L.; Prévôt, M. E.; Wakerlin, S. L.; Vanegas, J. P.; Salamonczyk, M.; Hegmann, E.; Zhu, C. H.; Wilson, M. R.; Jákli, A. I.; Hegmann, T. Heliconical-Layered Nanocylinders (HLNCs) Hierarchical Self-Assembly in a Unique B4 Phase Liquid Crystal Morphology. *Mater. Horiz.* **2019**, *6*, 959–968.
- (51) Shadpour, S.; Nemati, A.; Salamonczyk, M.; Prévôt, M. E.; Liu, J.; Boyd, N. J.; Wilson, M. R.; Zhu, C. H.; Hegmann, E.; Jákli, A. I.; Hegmann, T. Missing Link between Helical Nano- and Microfilaments in B4 Phase Bent-Core Liquid Crystals, and Deciphering Which Chiral Center Controls the Filament Handedness. *Small* **2020**, *16*, 1905591.
- (52) Liu, J.; Shadpour, S.; Prévôt, M. E.; Chirgwin, M.; Nemati, A.; Hegmann, E.; Lemieux, R. P.; Hegmann, T. Molecular Conformation of Bent-Core Molecules Affected by Chiral Side Chains Dictates Polymorphism and Chirality in Organic Nano- and Microfilaments. *ACS Nano* **2021**, *15*, 7249–7270.
- (53) Yang, D.; Duan, P. F.; Zhang, L.; Liu, M. H. Chirality and Energy Transfer Amplified Circularly Polarized Luminescence in Composite Nanohelix. *Nat. Commun.* **2017**, *8*, 15727.
- (54) Kim, B. C.; Choi, H. J.; Lee, J. J.; Araoka, F.; Choi, S. W. Circularly Polarized Luminescence Induced by Chiral Super Nanospaces. *Adv. Funct. Mater.* **2019**, 29, 1903246.
- (55) Liu, J.; Shadpour, S.; Nemati, A.; Prévôt, M. E.; Hegmann, E.; Zhu, C. H.; Hegmann, T. Binary Mixtures of Bent-Core Molecules Forming Distinct Types of B4 Phase Nano- and Microfilament Morphologies. *Liq. Cryst.* **2021**, *48*, 1129–1139.
- (56) Shadpour, S.; Nemati, A.; Liu, J.; Hegmann, T. Directing the Handedness of Helical Nanofilaments Confined in Nanochannels Using Axially Chiral Binaphthyl Dopants. *ACS Appl. Mater. Interfaces* **2020**, *12*, 13456–13463.
- (57) Hough, L. E.; Jung, H. T.; Kruerke, D.; Heberling, M. S.; Nakata, M.; Jones, C. D.; Chen, D.; Link, D. R.; Zasadzinski, J.; Heppke, G.; Rabe, J. P.; Stocker, W.; Korblova, E.; Walba, D. M.; Glaser, M. A.; Clark, N. A. Helical Nanofilament Phases. *Science* **2009**, 325, 456–460.
- (58) Jones, G. A.; Bradshaw, D. S. Resonance Energy Transfer: From Fundamental Theory to Recent Applications. *Front. Phys.* **2019**, *7*, 100.
- (59) Lee, M. H.; Kim, D.; Dong, Y. Q.; Tang, B. Z. Time-Resolved Photoluminescence Study of an Aggregation-Induced Emissive Chromophore. *J. Korean Phys. Soc.* **2004**, *45*, 329–332.
- (60) Wu, W. C.; Chen, C. Y.; Tian, Y. Q.; Jang, S. H.; Hong, Y. N.; Liu, Y.; Hu, R. R.; Tang, B. Z.; Lee, Y. T.; Chen, C. T.; Chen, W. C.; Jen, A. K. Y. Enhancement of Aggregation-Induced Emission in Dye-Encapsulating Polymeric Micelles for Bioimaging. *Adv. Funct. Mater.* **2010**, *20*, 1413–1423.

- (61) Time-Dependent Anisotropy Decays. In *Principles of Fluorescence Spectroscopy*, Lakowicz, J. R. (Ed.), Springer US: Boston, MA, 2006; pp 383–412.
- (62) Chen, D.; Zhu, C. H.; Wang, H. T.; Maclennan, J. E.; Glaser, M. A.; Korblova, E.; Walba, D. M.; Rego, J. A.; Soto-Bustamante, E. A.; Clark, N. A. Nanoconfinement of Guest Materials by Helical Nanofilament Networks of Bent-Core Mesogens. *Soft Matter* **2013**, *9*, 462–471.
- (63) Callahan, R. A.; Coffey, D. C.; Chen, D.; Clark, N. A.; Rumbles, G.; Walba, D. M. Charge Generation Measured for Fullerene-Helical Nanofilament Liquid Crystal Heterojunctions. *ACS Appl. Mater. Interfaces* **2014**, *6*, 4823–4830.
- (64) Baginski, M.; Tupikowska, M.; Gonzalez-Rubio, G.; Wojcik, M.; Lewandowski, W. Shaping Liquid Crystals with Gold Nanoparticles: Helical Assemblies with Tunable and Hierarchical Structures via Thin-Film Cooperative Interactions. *Adv. Mater.* 2020, 32, 1904581.
- (65) Choi, K. Y.; Han, J. J.; He, B.; Lee, S. B. Syndiotactic Polystyrene Nanofibrils in Silica Nanotube Reactors: Understanding of Synthesis with Ultrahigh Molecular Weight. *J. Am. Chem. Soc.* **2008**, 130, 3920–3926.
- (66) Li, A. P.; Muller, F.; Birner, A.; Nielsch, K.; Gosele, U. Hexagonal Pore Arrays with a 50-420 nm Interpore Distance Formed by Self-Organization in Anodic Alumina. *J. Appl. Phys.* **1998**, *84*, 6023–6026.
- (67) Dobriyal, P.; Xiang, H. Q.; Kazuyuki, M.; Chen, J. T.; Jinnai, H.; Russell, T. P. Cylindrically Confined Diblock Copolymers. *Macromolecules* **2009**, 42, 9082–9088.
- (68) Wu, Y. Y.; Cheng, G. S.; Katsov, K.; Sides, S. W.; Wang, J. F.; Tang, J.; Fredrickson, G. H.; Moskovits, M.; Stucky, G. D. Composite Mesostructures by Nano-Confinement. *Nat. Mater.* **2004**, *3*, 816–822
- (69) Chen, D.; Porada, J. H.; Hooper, J. B.; Klittnick, A.; Shen, Y. Q.; Tuchband, M. R.; Korblova, E.; Bedrov, D.; Walba, D. M.; Glaser, M. A.; Maclennan, J. E.; Clark, N. A. Chiral Heliconical Ground State of Nanoscale Pitch in a Nematic Liquid Crystal of Achiral Molecular Dimers. *Proc. Natl. Acad. Sci. U. S. A.* **2013**, *110*, 15931–15936.
- (70) Yoon, D. K.; Yi, Y.; Shen, Y. Q.; Korblova, E. D.; Walba, D. M.; Smalyukh, I. I.; Clark, N. A. Orientation of a Helical Nanofilament (B4) Liquid-Crystal Phase: Topographic Control of Confinement, Shear Flow, and Temperature Gradients. *Adv. Mater.* **2011**, 23, 1962–1967.
- (71) Kim, H.; Ryu, S. H.; Tuchband, M.; Shin, T. J.; Korblova, E.; Walba, D. M.; Clark, N. A.; Yoon, D. K. Structural Transitions and Guest/Host Complexing of Liquid Crystal Helical Nanofilaments Induced by Nanoconfinement. *Sci. Adv.* **2017**, *3*, 1602102.
- (72) Park, W.; Ha, T.; Kim, T. T.; Zep, A.; Ahn, H.; Shin, T. J.; Sim, K. I.; Jung, T. S.; Kim, J. H.; Pociecha, D.; Gorecka, E.; Yoon, D. K. Directed Self-Assembly of a Helical Nanofilament Liquid Crystal Phase for Use as Structural Color Reflectors. NPG Asia Mater. 2019, 11, 45
- (73) Gao, Y. Z.; Yao, W. H.; Sun, J.; Li, K. X.; Zhang, L. Y. Angular Photochromic LC Composite Film for an Anti-Counterfeiting Label. *Polymer* **2018**, *10*, 453.
- (74) Schwartz, M.; Lenzini, G.; Geng, Y.; Ronne, P. B.; Ryan, P. Y. A.; Lagerwall, J. P. F. Cholesteric Liquid Crystal Shells as Enabling Material for Information-Rich Design and Architecture. *Adv. Mater.* **2018**, *30*, 1707382.
- (75) Geng, Y.; Noh, J.; Drevensek-Olenik, I.; Rupp, R.; Lenzini, G.; Lagerwall, J. P. F. High-Fidelity Spherical Cholesteric Liquid Crystal Bragg Reflectors Generating Unclonable Patterns for Secure Authentication. *Sci. Rep.* **2016**, *6*, 26840.
- (76) Tsai, E.; Richardson, J. M.; Korblova, E.; Nakata, M.; Chen, D.; Shen, Y. Q.; Shao, R. F.; Clark, N. A.; Walba, D. M. A Modulated Helical Nanofilament Phase. *Angew. Chem., Int. Ed.* **2013**, *52*, 5254–5257.
- (77) Keene, D. R. A Review of Color Blindness for Microscopists: Guidelines and Tools for Accommodating and Coping with Color Vision Deficiency. *Microsc. Microanal.* **2015**, *21*, 279–289.